International Journal of Plasticity 83 (2016) 19–36

Contents lists available at ScienceDirect

International Journal of Plasticity

journal homepage: www.elsevier.com/locate/ijplas

# Three dimensional quantification of anisotropic void evolution in deformed semi-crystalline polyamide 6

Lucien Laiarinandrasana [a,*], Olga Klinkova [a], Franck Nguyen [a], Henry Proudhon [a], Thilo F. Morgeneyer [a], Wolfgang Ludwig [b]

[a] MINES ParisTech, PSL-Research University, MAT-Centre des Matériaux, CNRS UMR7633, BP 87, F-91003 Evry Cedex, France
[b] European Synchrotron Radiation Facility (ESRF), BP 220, F-38043 Grenoble Cedex, France

ARTICLE INFO

*Article history:*
Received 12 October 2015
Received in revised form 1 April 2016
Available online 14 April 2016

*Keywords:*
A. Voids and inclusions
B. Finite strain
B. Polymeric material
B. Porous material
C. Finite elements

ABSTRACT

The evolution of voids has been used as an efficient indicator of the volume changes occurring during deformation for polymers which undergo high levels of plasticity. This has to be taken into account in determining the constitutive models for these polymers. Void growth during uniaxial stretching of a semi-crystalline polyamide 6 has been studied using 3D image analysis of tomography data. Tests on axi-symmetrical notched round bars have been stopped at: (i) the maximum net stress; (ii) the end of the stress softening stage; (iii) the onset of the final failure. Local synchrotron tomography has been performed so as to observe voids in a predetermined volume of interest around the minimum net section. The shape of the voids was found to be cylindrical. Mathematical morphology analysis was used to identify 3D voids, allowing the void diameter and height histograms to be obtained. An anisotropic shape factor parameter was defined as the ratio between the void diameter and the void height. This shape factor was found to evolve with the degree of deformation. The principal strain components of the voids were calculated and plotted, showing anisotropy and a heterogeneous distribution. The irreversible void growth noted as plastic dilation was also found to be heterogeneous in the deformed net section.

© 2016 Elsevier Ltd. All rights reserved.

## 1. Introduction

The demand for thermoplastic polymers has been increasing continuously over the last few decades, essentially due to their low density, ease of processing and also due to environmental constraints. Even composite materials, most often made with thermosetting matrices are increasingly designed with thermoplastic polymers. The assessment of the structural integrity of components made of these materials is of prime importance so as to ensure in-service security and to predict the durability of their use. To this end, their mechanical response has been studied in order to establish a reliable constitutive model that accounts as much as possible for any evolution of the microstructure. Usually, the mechanical response of a given material is studied by using essentially macroscopic data such as the load and, in the best case, full field displacement at the external surface of the specimen.

In terms of microstructure examinations, the Peterlin–Schultz (Peterlin, 1971; Schultz, 1974) mechanisms based on the highly fibrillated matter due to crystallite tilting during previous hardening were for a long time a motivation for various

* Corresponding author. Tel.: +33 1 60 76 30 64; fax: +33 1 60 76 31 50.
*E-mail address:* lucien.laiarinandrasana@mines-paristech.fr (L. Laiarinandrasana).

http://dx.doi.org/10.1016/j.ijplas.2016.04.001
0749-6419/© 2016 Elsevier Ltd. All rights reserved.

inspection techniques. In a non exhaustive way, basic surface observations were carried out using optical microscopy, scanning electron microscopy (SEM) or transmission electron microscopy (TEM). These techniques require tedious and destructive surface preparations (microtome cutting or cryofracture followed by etching) that induce observation artefacts. A second category of observation techniques give an access to internal and volumetric information:

- Short Angle X-ray Scattering (SAXS) (Butler et al., 1998; Pawlak and Galeski, 2008; Castagnet et al., 2000; Hughes et al., 1997);
- Incoherent Polarized Steady Light Transport (IPSLT) (Farge et al., 2013);
- Raman spectroscopy (Chaudemanche et al., 2014) coupled with VidéoTraction ™.

Using these techniques, nanovoids can be detected and characterized by averaging them within a volume of a few $mm^3$. Most of the studies reported clustering of these nanovoids giving rise to the existence of an anisotropy index which evolves during a uniaxial tensile test (Farge et al., 2013; Xiong et al., 2013). Although these techniques provide very local information at a nanoscopic scale of the microstructure, the precise locations of nanovoids cannot be well established.

The objective of this work was to better understand the void growth mechanisms during stretching of a semi-crystalline polyamide 6. Synchrotron Radiation Tomography (SRT) was used for the inspection of the microstructure. An innovative experimental method is proposed to relate the microscopic tomography analysis (with submicron spacial resolution) to the macroscopic properties of the polyamide 6 under study. Void shape and volume have been measured by SRT image analysis resulting in comprehensive statistical data, spread within the volume of the deformed sample. Thanks to the concept of a volume of interest (VOI), the distribution of these data through the thickness of the material has been plotted at each level of applied macroscopic deformation. Therefore, the deformation heterogeneity or gradient through the thickness of the sample could clearly be highlighted. It is now well established that constitutive models should be based on the relationships between deviatoric as well as hydrostatic stresses and strains. 3D characterization of volumetric strain is useful in improving the reliability of the FE models used to assess the durability of engineering structures made of polymers.

The first part of the paper gives details of the material and the specimens which have been studied. The experimental procedure is then described, showing both the three specific deformation stages that have been analyzed and also the macroscopic data obtained. At the microscopic scale, the SRT setup is summarized and the volumes of interest are defined. The following sections focus on two kinds of results:

- Qualitative information relative to micro-mechanisms: describe the cylindrically shaped voids. The micromechanisms of void deformation are discussed in terms of void morphology and arrangement. To better analyze these qualitative data and to initiate the quantification processes, statistical figures (histograms) on void height and diameter over the volumes of interest are given;
- Quantitative data to be linked to the deterministic mechanical parameters: the mode values (maximum frequency) of void height and void diameter were selected in order to allow the distributions within the deformed net section to be plotted.

The last section of the paper gives details of the calculation step allowing the void strain tensor to be evaluated. The distributions of the axial, radial and volumetric strains within the deformed net section are then discussed.

## 2. Material and experimental procedures

The material under study was a semi-crystalline thermoplastic polyamide 6 (PA6) (Regrain et al., 2009; Cayzac et al., 2013). The main physico-chemical characterictics are recalled here: the glass transition temperature $T_g = 53$ °C, the melting point temperature $T_m = 219$ °C and the crystallinity index $\chi = 43\%$ have been determined by Modulated Differential Scanning Calorimetry (MDSC). The spherulitic microstructure was observed by Scanning Electron Microscopy (SEM) after chemical etching. A spherulite mean diameter of 5 μm was then measured. To study the damage mechanisms, cryo-fractured samples allowed SEM examination of PA6 brittle fracture surfaces (Laiarinandrasana et al., 2010). Image analysis was carried out on several SEM images allowing estimates of the initial void volume fraction at about 1% and a mean void diameter of around 0.1 μm.

As already mentioned, the present work is devoted to the study of the evolution of voids within notched round bars (Fig. 1a) subjected to tensile loads. The initial notch root radius was 4 mm (R4) and the initial vertical distance between the notch shoulders $\delta_0 = 3$ mm. The advantage of such a geometry is that the cross section in the notched region of the specimen is subjected to a triaxial stress state that can be theoretically characterized (Cayzac et al., 2013).

### 2.1. Data at the macroscopic scale

The above mentioned notched round bars (Fig. 1a) were tested at room temperature (20 °C) with an electromechanical tensile rig with a controlled crosshead speed of 0.08 mm/s. The experimental procedure consisted of, first carrying out a tensile test up to the failure of the specimen, in order to plot the general trends of the load versus applied displacement curves

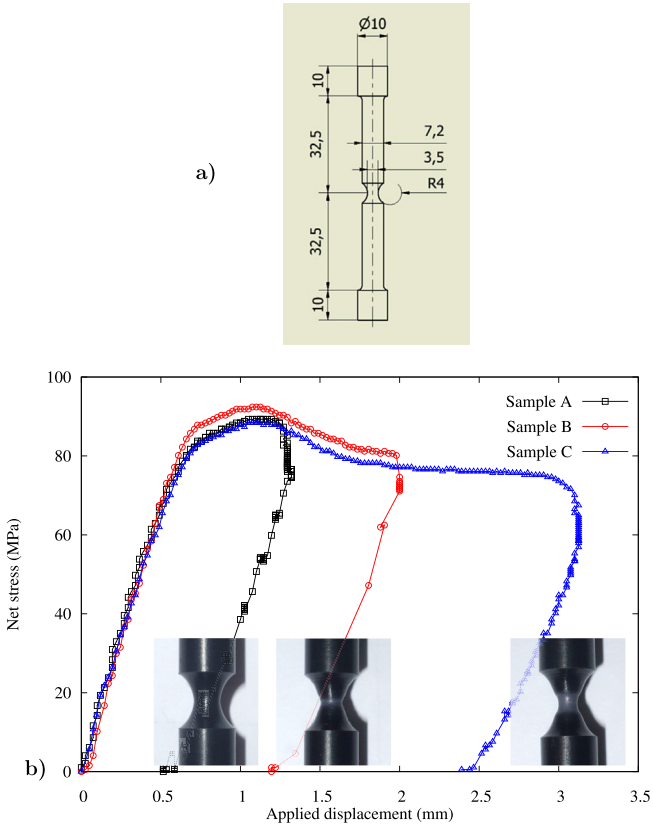


**Fig. 1.** Sample preparations: a) Notched round bar with characteristic dimensions and notch root radius equal to 4 mm; b) net stress *vs.* applied displacement curves with deformed samples A, B and C (after Laiarinandrasana et al. (2012)).

(Cayzac et al., 2013). Then, tests were stopped at the three characteristic points so as to follow the evolution of the microstructure. For the sake of reproducibility, each of these tests was repeated at least twice.

The curves relating the engineering net stress ($F/S_0$) where F is the load and $S_0$ is the net section area, as a function of applied crosshead displacement ($\Delta\delta$) are illustrated in Fig. 1b. Pictures of the deformed samples, around the notched regions are also provided. For sample A, the test was stopped at the peak value of the net stress. Then the unloading was carried out with the same controlled crosshead speed of 0.08 mm/s leading to a residual displacement equal to 0.6 mm. The same operation was carried out for samples B and C for which tests were interrupted after the post-yielding stress-softening (decrease of the net stress) stage and at the end of the stress plateau, with residual displacements of 1.2 mm and 2.4 mm respectively.

As shown in Fig. 1b, sample A did not change in aspect whereas samples B and C exhibited necking accompanied by whitening at their minimal cross sections. Measurements of the characteristic lengths of the deformed samples were carried out. Fig. 2a shows details of the definitions of these measured lengths as follows: $h_w$ is the height of the whitened zone, $r_s$ is the actual net section radius and for the sake of simplicity the notch opening displacement —based on $\delta_0$ and noted as $\Delta\delta_p$— is considered as the residual displacement. The values for each sample are given in Table 1. They remained constant for several months after the tests. They are considered as irreversible/permanent sets. It is to be noted that for sample A, $h_w$ is zero.

### 2.2. Data at the microscopic scale

#### 2.2.1. Synchrotron Radiation Tomography (SRT) setup and data treatment

After at least two months in an unloaded free state (stress recovery), the three deformed samples A, B and C were subjected to standard parallel beam SRT at the European Synchrotron Radiation Facility (ESRF), beamline ID19. Tomography, which is analogous to the better known X-ray medical scanner, is based on the acquisition of many transmission X-ray radiographies while the samples rotates. The SRT setup was described in Laiarinandrasana et al. (2012): an energy of 17.6 keV was used. 1500 radiographs were recorded continuously through a 180° rotation. Exposure time was set to 0.1 s, resulting in a scan duration of 3 min and a voxel size of 0.7 μm. The 3D spatial distribution of the X-ray attenuation inside the sample was computed. An image of the density distribution of the sample and thus of the internal microstructure was obtained in a non destructive manner within a total scanned volume of about 1 $mm^3$.

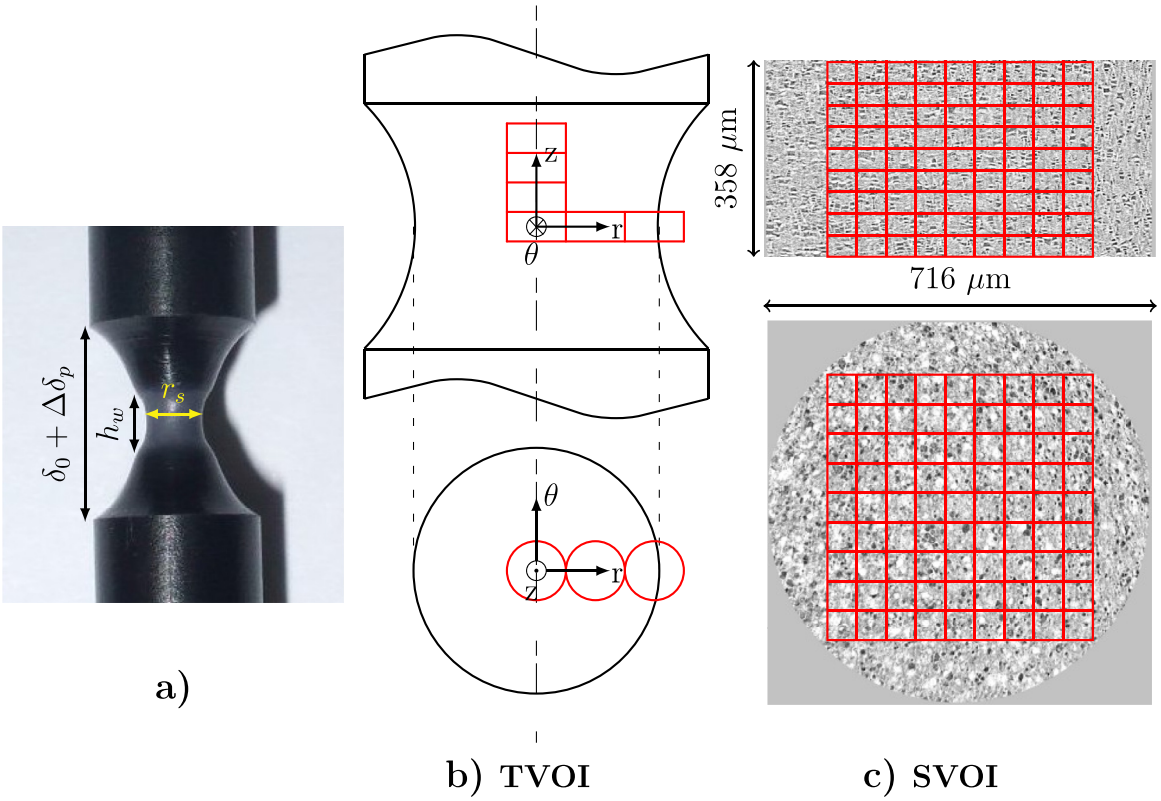


**Fig. 2.** Sample details for tomographic inspections: a) Definition of $\delta_0, \Delta\delta_p, r_s, h_w$ (Table 1) on the deformed sample C; b) locations of the cylindrical (diameter = 716 μm, height = 356 μm) Tomographic Volumes Of Interest (TVOI) defined during local tomography inpections; c) description of parallelepipedic Statistical Volumes Of Interest (SVOI) within the TVOI.

**Table 1**
Height of the whitened zone ($h_w$), deformed section radius ($r_s$) and permanent notch opening displacement ($\Delta\delta_p$) measured at the macroscopic scale (surface), with initial lengths: $\delta_0 = 3$ mm and $r_0 = 1.75$ mm. Definitions in Fig. 2.

| | $h_w$ (mm) | $r_s$ (mm) | $\Delta\delta_p$ (mm) |
|---|---|---|---|
| Sample A | 0 | 1.69 | 0.6 |
| Sample B | 1.08 | 1.38 | 1.2 |
| Sample C | 2.6 | 1.16 | 2.4 |

As already mentioned, image analysis has been carried out on the reconstructed images using mathematical morphology concepts (Serra, 1988). An image is represented by its own grey level histogram containing some artefacts and typically non uniform brightness. The voids which are dark have to be identified by the **local minima** of a continuous distribution function to be optimized. To collect these local minima, an efficient algorithm proposed by Beucher (1990) was used. Finally, the binarization of the data allows the labelling of each void together with detailed figures such as the coordinates of the centre, the volume and the morphology. Locating each void inside the volume is of prime importance in the following. Indeed, unlike other examination techniques delivering an average value of void properties through the volume, data processed here allows the distribution of these individual void dimensions to be plotted.

### 2.2.2. Volumes of interest

The inspected volumes have to be determined so as to relate them with the microstructural characteristic lengths. Fig. 2 introduces two volumes of interest. In the aforementioned setup the material volume contributing to the projection had a diameter of about 3 mm. By using a local tomography technique (Laiarinandrasana et al., 2010, 2012; Morgeneyer et al., 2014) the size of the field of view was only 716 μm in diameter and 358 μm in height (Figs. 2b–c). This volume will be described as the tomographic volume of interest (TVOI). Fig. 2b reveals the locations of the TVOI illustrated as open circles in the horizontal cut $(r, \theta)$ view and as open rectangles in the longitudinal $(r, z)$ view, respectively. In practice, the acquired data sets consist of a maximum of 7 and 4 TVOI along z- and r-directions, respectively. Note that the point of reference is the central point of the sample located by $z = r = 0$ in cylindrical coordinates as described in Fig. 2b.

It was shown that the void morphological parameters showed gradients through the thickness of the TVOI. A statistical volume of interest (SVOI) is introduced here. In Laiarinandrasana et al. (2012) it consisted of 3 × 3 small parallelepiped volumes virtually cut within the TVOI. Each SVOI was then registered into the deformed specimen coordinates system as depicted in Fig. 2b–c by using the macroscopic measure of the deformed section radius ($r_s$), see Table 1.

In the present work, a study of the influence of the SVOI size was carried out. It consisted of comparing data from 3 × 3 SVOI with those corresponding to 9 × 9 SVOI. It was seen that for void diameter and height modes, reducing the number of SVOI (increasing their size) resulted in a smaller scatter as well as a slight decrease of the mean value. In order to keep the same sampling over the net section as that corresponding to the steepest gradient in the vicinity of the notch root, refined sampling was required. Therefore a total of 9 × 9 parallelepiped SVOI were chosen as illustrated in Fig. 2c. Each SVOI then had a size of (50 μm × 50 μm × 40 μm) which would contain an average of 150 spherulites. Statistical data were collected inside each SVOI which was related to its centre so as to refer to the actual coordinates within the whole sample.

## 3. Results

This section describes the results of the microscopic inspections, initially in a qualitative fashion, showing the morphology and the organization of the voids. These features are then characterized by plotting histograms obtained from each SVOI. In the following section, a quantitative analysis of the voids; mode heights and diameters is performed so as to better understand their evolution during the deformation of the specimen.

### 3.1. Morphology of voids – polar fans

Qualitative results from SRT inspections are reproduced in Fig. 3. For each sample, a cube of $(140\ \mu m)^3$ was extracted from the central TVOI. Voids are in black whereas the matrix is in grey. Some matter in a lighter grey can be distinguished (even in white), corresponding to intervoid walls as already reported by Laiarinandrasana et al. (2010, 2012). The initial load direction was vertical, normal to the penny shaped voids seen for Sample A for instance.

For sample A, voids were close to being penny shaped. Black patterns are circular in the horizontal section but are represented by lines in the section normal to the specimen radius. This morphology can be described as cylindrical like shapes where the height is less than the diameter. The intervoid walls have a larger height than the voids. The side view of these voids is similar to that which was identified as crazes in many semi-crystalline polymers (Laiarinandrasana et al., 2012) by using SEM examinations. Actually, microfibrils are presumably present within the voids here but cannot be resolved due to the detection limit. Farge et al. (2013), by using IPSLT and SAXS techniques reported that the medium is composed of nanovoids and destructured fibrils of matter. From the deformed state of sample B, these fibrils are no longer visible. For the sake of simplicity, it can be assumed that even for sample A the dark penny shaped objects were voids and not crazes.

From sample A to sample B, that is during the stress-softening, voids were observed to extend in height. It seems also that the height of intervoid walls decreased simultaneously. Consecutively, sample C seems to have followed this micromechanism process: void height extension with a decrease in wall height accompanied by shrinking of the diameter. This void morphology in sample C is consistent with what has been observed by Pawlak and Galeski (2008, 2010) and Rozanski and Galeski (2013) and identified as damage initiation in polar fans of the spherulite.

So as to examine more closely this arrangement of voids in columns, two polar fans have been selected in the central axis of sample C but at two locations along the load axis: Fig. 4a shows images near the neck shoulder ($z > 0$) whereas Fig. 4b was located at a central part corresponding approximately to $z = 0$. It can be noticed that the evolution of height and diameter was

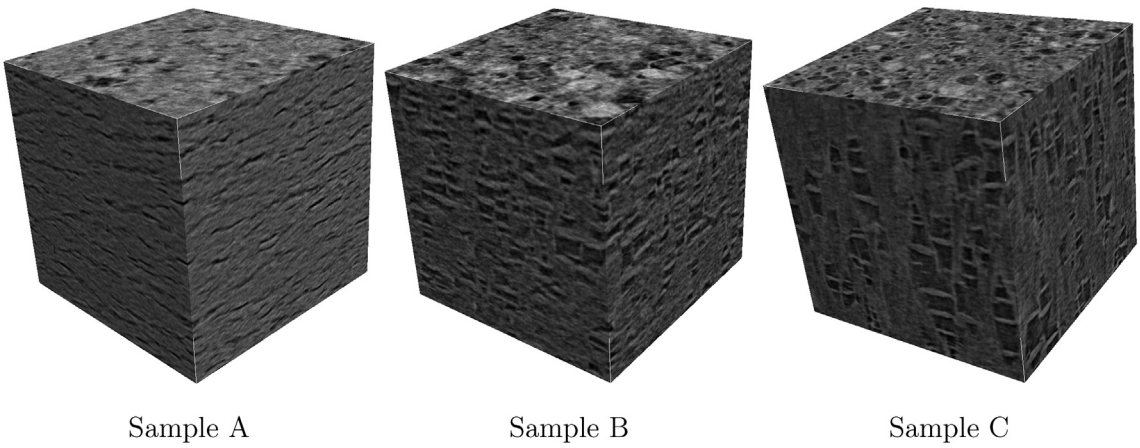


**Fig. 3.** Morphology of voids depending on the deformation before unloading. Box size = $(140\ \mu m)^3$ (after Laiarinandrasana et al. (2012)).

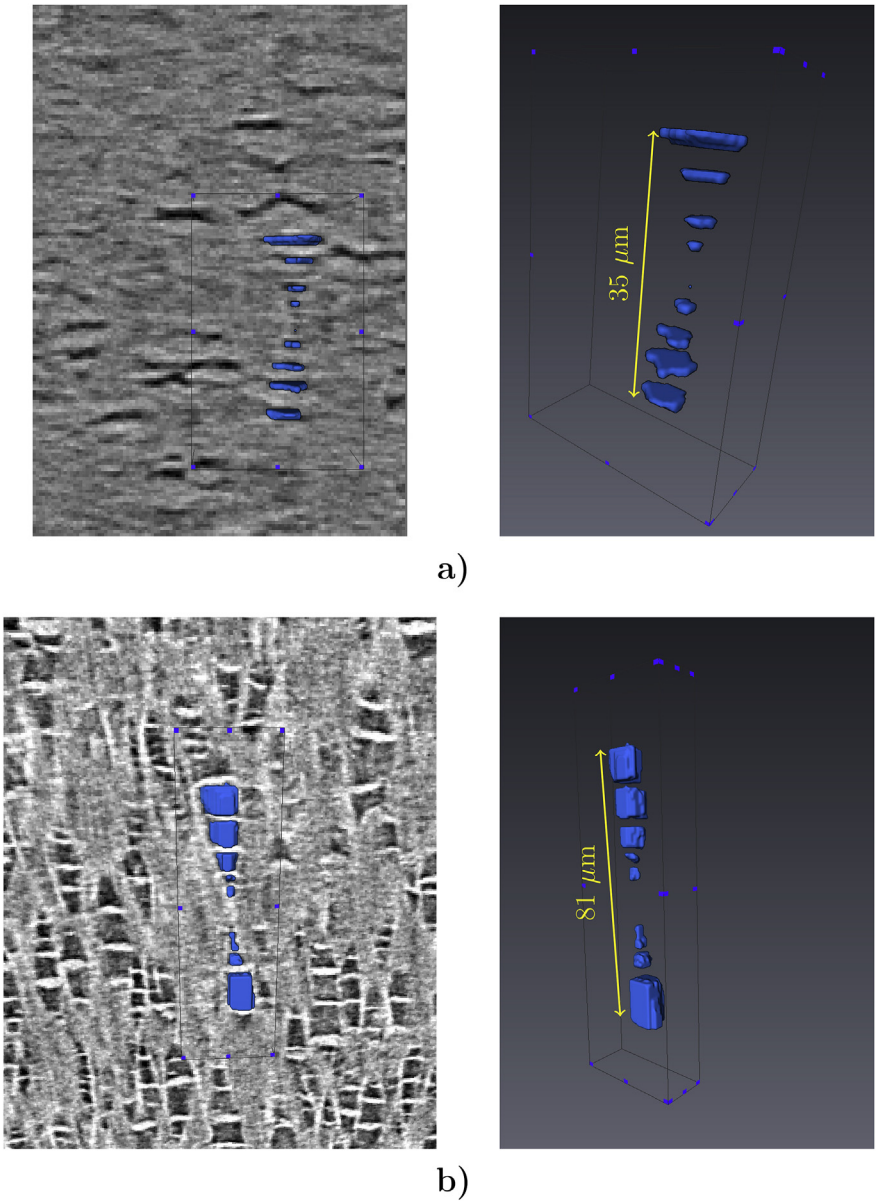


**Fig. 4.** Images from central zones of sample C showing the details of void morphology arranged as polar fans (consistent with Rozanski and Galeski (2013)): a) small deformation as disks near the neck shoulder; b) high deformation as cylinders in the necked zone.

similar to that which was observed for the three samples A, B and C, that is at various deformation states. Following the description of polar fans, it is assumed here that the vertex (conical void) indicates the centre of a spherulite (although the boundaries of the spherulites were not revealed here) whereas the base of the fan was located approximately at the interface between two spherulites packed in a column. In Fig. 4a, considering that the maximum diameter represents the spherulitic interfaces, this deformed spherulite would have a height of about 35 μm. Unfortunately the initial height of this spherulite is not known, so that the deformation of this spherulite could not be evaluated. In the central part $z = 0$ (Fig. 4b), the total height of the indicated polar fan is about 81 μm. By assuming that the initial height of this spherulite is of 35 μm, as observed previously in the neck shoulder (gauge length), the relative axial deformation of this spherulite can be estimated at about 130%. This gives an idea of the large deformation to which the material is subjected on a local scale.

To cross-check the results that will be presented by data processing below, the ranges of height and diameter for individual voids in Fig. 4 were measured, yielding:

– Fig. 4a: height $\simeq$ 2 μm; 2 μm $\leq$ diameter $\leq$ 8 μm

– Fig. 4b: 3 μm ≤ height ≤ 12 μm; 3 μm ≤ diameter ≤ 9 μm

These values were collected within a volume located at 140 μm from the *z*-axis.

### 3.2. Histograms of void heights and diameters

Since voids are cylindrically shaped, the projections of the minimum and maximum lengths on the fixed macroscopic coordinate axes as skecthed in Fig. 2 were recorded. These measures called Feret dimensions (Feret, 1930) are relevant when the items do not rotate during the deformation. The lengths in the directions of *z*-axis and *r*-axis are considered as the height ($h$) and diameter ($\phi$) respectively. Since, rotation of voids was observed in a layer very close to the notch root surface, uncertainties on the measured lengths are increased in these areas.

With the data collected, the histograms of each of the 81 SVOI included in each TVOI could be plotted. The central SVOI of each sample was selected here as an example to illustrate the approach. Actually, for each sample the histograms corresponding to the SVOI located in the central position of the central TVOI was plotted in Fig. 5. From the top to the bottom

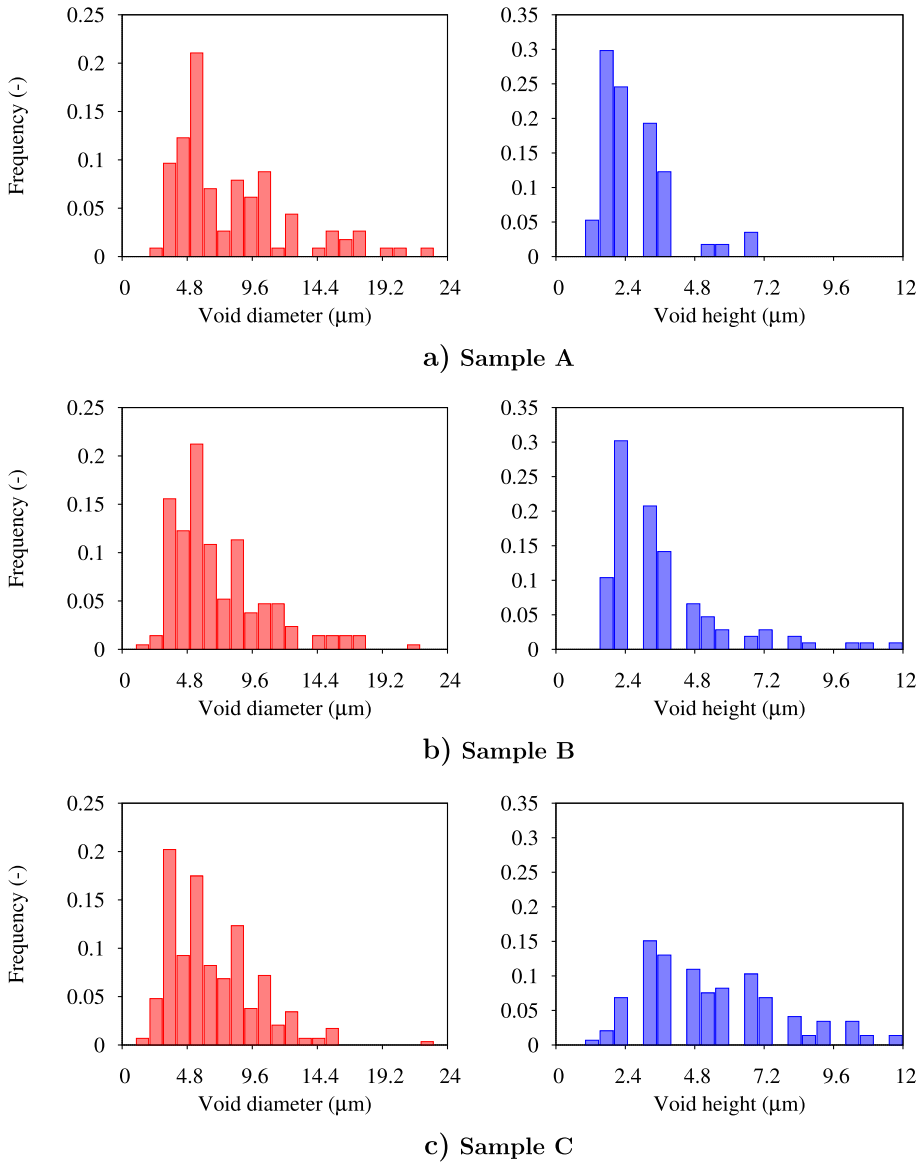


**Fig. 5.** Histograms of void height and diameter for the central SVOI in the central TVOI for samples A, B and C. (*N.B.: i) The frequency is defined as the ratio between the number of voids with the class of diameter/height and the total number of voids within the SVOI; ii) The mode value (length corresponding to the maximum frequency) is included in the class related to the maximum cumulative frequency in the above histograms*).

positions graphs are displayed from sample A to sample C. In the left part of Fig. 5 are shown the histograms of diameter, the right part gives the histograms of void heights.

For each histogram, a population of about one hundred cavities has been analyzed. Various statistical parameters in terms of height and diameter are available in the literature. For instance, Landron et al. (2011) analyzed the influence of the number (1, 20, 50, overall data) of largest cavities so as to process their data: the maximum value was then obtained. In the present work, the maximum and minimum values were subjected to uncertainties. The minimum value was affected by the resolution and the segmentation parameters whereas the maximum length was biased by the inability of the Feret measure to separate two (or more) joined radial voids and to ignore projections of inclined voids. Therefore, attention was then paid to classical statistical variables:

- the *mean value* is the average length calculated using the overall data. This parameter was found to exhibit the largest uncertainties due to the cumulated influence of uncertainties related to the minimum and maximum lengths;
- the *median value* is related to a cumulated frequency of 50% by counting for increasing length (starting from the minimum length). Due to the profile of the histograms, the median value is systematically larger than the mode value. In addition this value is greatly influenced by the minimum length;
- the *mode value* is the length corresponding to the maximum frequency (mode = most often). This latter variable was selected here since it seemed to be the most relevant for the qualitative observation.

Indeed, in Fig. 5, the maximum frequency can vary from more than 30% to only about 15% between sample A and sample C, but the void mode diameter and mode height seem to follow the previous qualitative observations (Section 3.1). The maximum cut-offs on the X-axis were adjusted from measured data: 12 μm in height and 24 μm in diameter. The minimum values were determined according to the resolution and the segmentation operations (threshold): about 1 μm in height and 2.5 μm in diameter. The maximum frequencies, allowing for the determination of the mode values, did not exceed 30% for the height and 22% for the diameter.

**From sample A to sample B** the mode diameter of 5.25 μm remained unchanged during the extension whereas the mode height increased from 1.75 μm to 2.3 μm (Fig. 5b). This would mean that for voids located in the central part of the initially notched specimens, the transformation from the peak stress to the end of the stress softening consisted of an elongation in the direction of the applied load **without any lateral deformation**. In other words, voids were subjected to an axial volumetric deformation (void growth).

**From sample B to sample C** (stress plateau) the mode height continued to increase and the mode diameter decreased as expected. Depending on the magnitude of the diameter contraction, voids could exhibit growth, isochoric deformation or closure, that will be quantified later.

Other SVOI histograms were analyzed but they are not shown here. Table 2 summarizes results obtained for the SVOI located near the notch surface. For samples A, B and C, the diameter continuously decreased, respectively: 5.25 μm, 4.85 μm and 3.50 μm whereas the height increased: 1.75 μm, 3.15 μm and 4.55 μm respectively. In this region, voids could be subjected to a slight diametrical reduction accompanied by large height extension. This might have led to a void growth larger than that located in the centre. Therefore, the maximum void growth might be located elsewhere other than in the central part (see Table 3).

Histograms corresponding to voids within an axial SVOI located near the notch shoulder show that neither the mode diameter (5.25 μm) nor the mode height (1.75 μm) was changed during the extension through samples A to C. Although the exact location of the axial SVOI is not the same within the samples due to the extension of the neck shoulder, it can be concluded that near the neck shoulder voids neither evolve in height nor in diameter. They remain penny shaped during the extension.

A complex void deformation field is observed within the necked region. It corresponds to a change from pure volumetric strain in the centre to a straining relative to a uniaxial stress near the notch root or even to a no deformation mode in the neck shoulder. To better understand this variation, the spacial distributions of the mode diameters and mode heights along the $r$ and $z$ axes have to be plotted. To this end, they were selected and related to the coordinates of the centre of each SVOI.

### 3.3. Evolution of voids mode height and diameter

Attention has been first paid to the evolution of the diameters and heights for SVOI aligned along the $z$ load-axis (Fig. 6). To the authors' best knowledge this is the first time that such experimental curves relative to void mode diameter and mode

**Table 2**
Mode values of void diameter and height for a radial SVOI located in between the centre and the notch surface for samples A to C.

| | Mode diameter (μm) | Frequency | Mode height (μm) | Frequency |
|---|---|---|---|---|
| Sample A | 5.25 | 0.27 | 1.75 | 0.47 |
| Sample B | 4.85 | 0.38 | 3.15 | 0.23 |
| Sample C | 3.5 | 0.22 | 4.55 | 0.14 |

**Table 3**
Mode values of void diameter and height for a axial SVOI located near the notch shoulder for samples A to C.

| | Mode diameter (μm) | Frequency | Mode height (μm) | Frequency |
|---|---|---|---|---|
| Sample A | 5.25 | 0.27 | 1.75 | 0.50 |
| Sample B | 5.25 | 0.18 | 1.75 | 0.50 |
| Sample C | 5.25 | 0.18 | 1.75 | 0.25 |

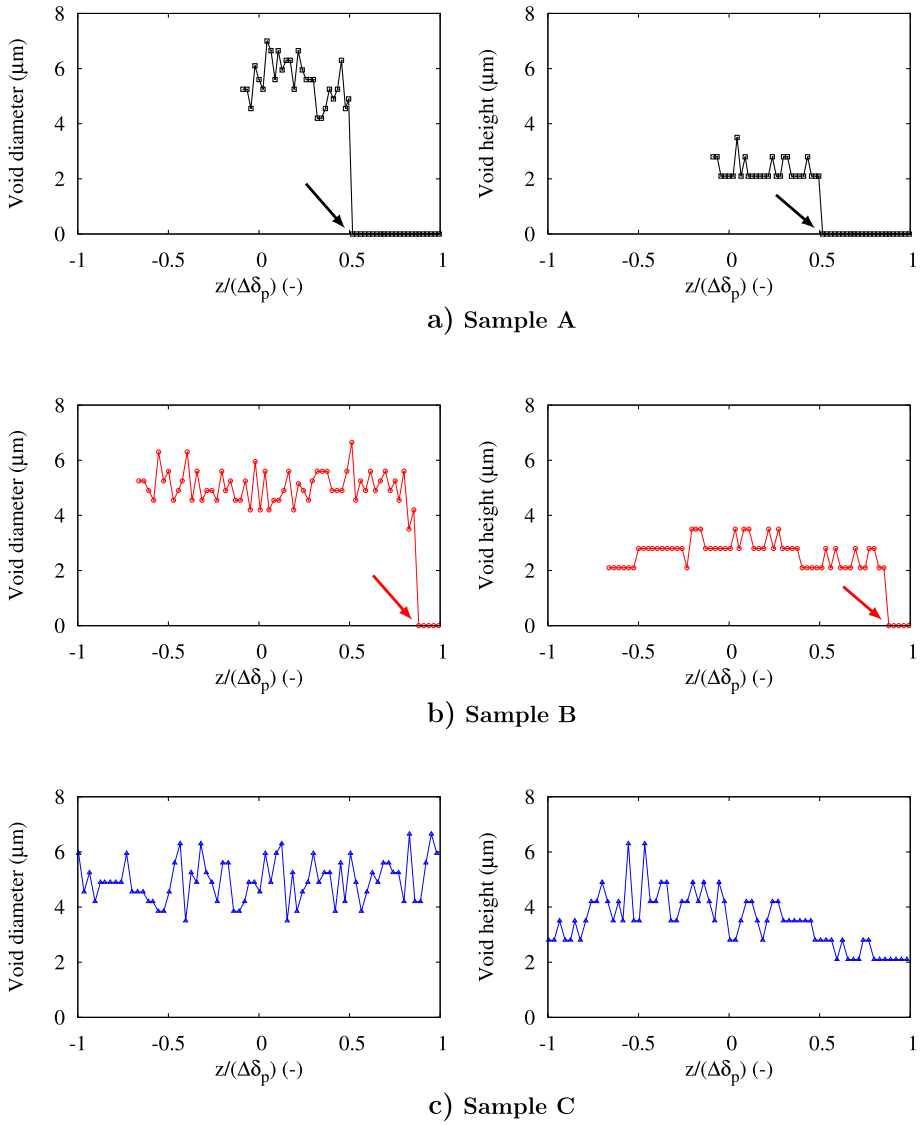


**Fig. 6.** Axial evolution of void height and diameter for increasing load corresponding respectively to $\Delta\delta_p = 0.6$ mm, 1.2 mm and 2.4 mm for samples A, B and C. *(Arrows indicate the end of the voided regions).*

height have been plotted for polymers. Indeed, this kind of statistically relevant distribution data can only be accessed in a non destructive way by the tomography technique, that is, without cutting, etching or coating operations needed before SEM examinations.

Fig. 6 displays, from the top to the bottom, the void diameter (left) and height (right) modes. The $z$ coordinate is normalized here by the permanent set ($\Delta\delta_p$) given in Table 1. The diagrams were set to the same scale for comparison purposes.

The normalized radii where the void diameter and height drop (see arrows in Figs. 6a and b) indicate approximately the height of the voided zones in sample A and sample B, whereas for sample C, the number of TVOI along the $z$-axis was not

sufficient to observe this drop off. These local heights of voided zone were measured and gave results of 0.3 mm, 1.08 mm and larger than 2.4 mm respectively for samples A, B and C. Except for sample A, for which no visible whitening could be seen, these values coincide with the heights of the whitened zone ($h_w$ in Table 1) measured at the surface and equal respectively 1.08 mm and 2.6 mm. For the PA6 polymer under study, once the whitening was visible at the surface, it could be taken as a signature of cavitation inside the material. The extent of voided zone could be evaluated by measuring the size of the whitened zone.

A slight gradient can be noticed in the diameter distribution for sample A and in the void mode height distributions for samples B–C. Elsewhere, homogeneous lengths were observed over the net sections. The decrease in diameter (from top to bottom left) accompanied by the height increase (from top to bottom right) from sample A to sample C shows the evolution of the void shape: starting from disks to cylinders with similar values of the height and the diameter.

Fig. 7 displays the data in the same way as in Fig. 6. At this stage, focus is only put on experimental data plotted using open symbols. The lines labelled "fit sample X" (X = A, B or C) will be discussed later in section 4.1. The left diagrams in Fig. 7 show the radial evolution of the void diameter. The profile is like an inverted parabola for sample A, flattened in the centre for sample B and "M-shaped" for sample C. Hence, the maximum value is located in the centre for samples A and B, but situated at about $r/r_s \simeq \pm 0.6$ for sample C. This configuration has already been reported by Brusselle-Dupend et al. (2011) for tomographic observation on PVDF polymer. As mentioned previously, this maximum value did not vary so much for sample A to sample B but slightly decreased from sample B to sample C.

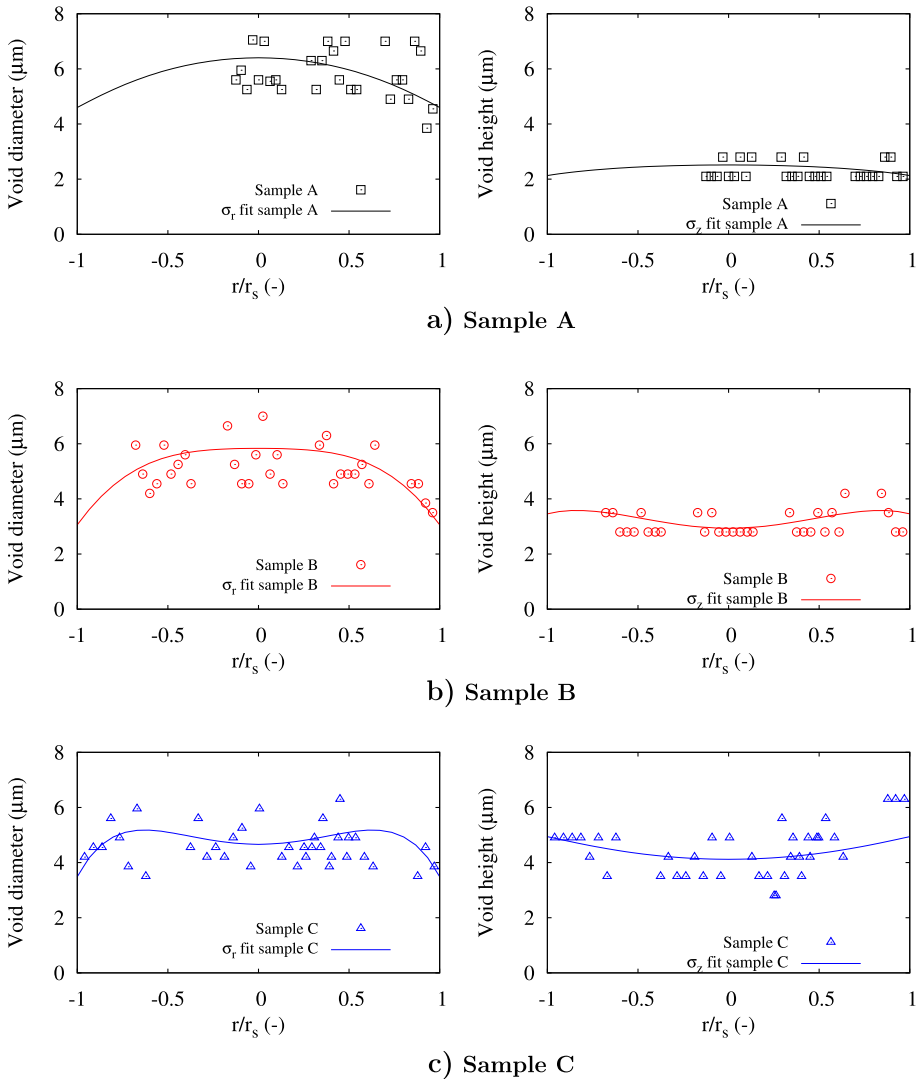


**Fig. 7.** Radial evolution of void diameter and height for increasing load corresponding respectively to $r_s = 1.69$ mm, 1.38 mm and 1.16 mm for samples A, B and C. Fitting of void diameter and height using radial ($\sigma_r$) and axial ($\sigma_z$) stress trends respectively.

The radial distribution of the void heights (Fig. 7 right) shows parabolic profiles, except for sample A that seems to have a homogeneous height of about 2.5 μm through the net section. Increasing the applied extension results in increasing both the minimum value of the height (located in the centre of the specimen) and the variation of the height from the centre to the surface.

These evolutions again highlight the various kinds of void deformation depending on to the applied extension as well as its location in the net section:

- around the centre: an oriented volume increase (increasing height for a fixed value of the diameter) from sample A to B followed by a common deformation mode (height increase, diameter decrease) from sample B to C;
- near the notch root: the same mode of void deformation from sample A to C, consisting of continuous increase (*resp.* decrease) of the height (*resp.* diameter);
- a complex situation at $r/r_s \simeq \pm 0.6$.

### 3.4. Void shape factor

This section goes further into highlighting the observed anisotropy. Data collected in the previous sections have been rearranged in order to obtain an anisotropic parameter noted as the shape factor ($S_f$), defined as the ratio between the mode diameter $\phi$ and the mode height $h$. This definition implies that a large $S_f$ corresponds to penny shaped (disk, oblate) voids whereas if $S_f = 1$, voids show a cylindrical shape for which the height equals the diameter. It is to be pointed out that here a shape factor of one does not mean a spherical void. When $S_f \leq 1$, voids are cylindrical and elongated in the direction of the applied load (cigar, prolate void).

Fig. 8a illustrates the radial distributions of $S_f$ for the three samples. In this section, only experimental data (full symbols) are considered. In spite of the large scatter band (oscillations) the general profile of the distribution can be described by an

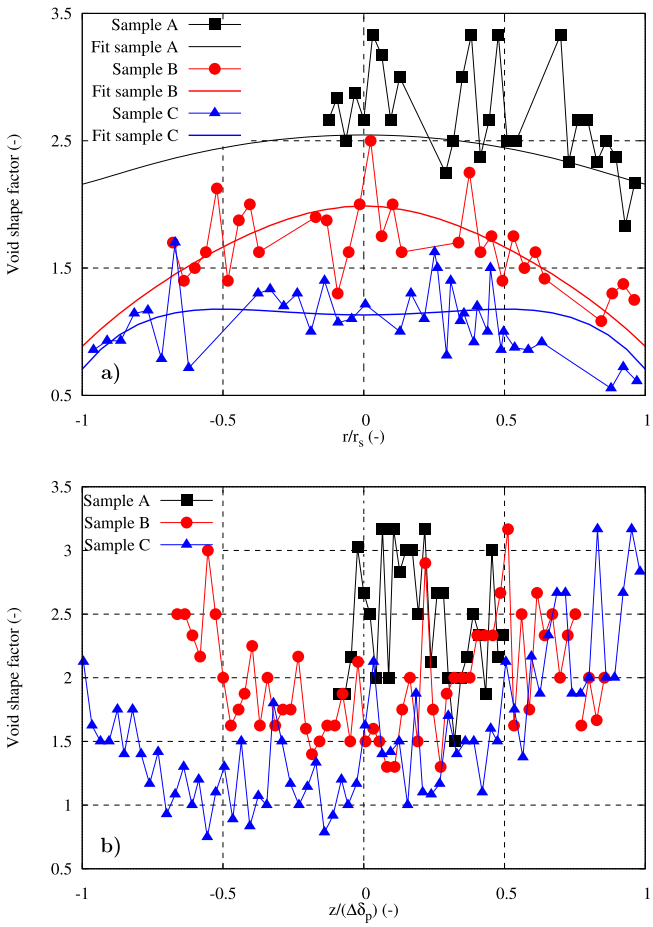


**Fig. 8.** Spacial distributions of void shape factor (diameter/height): a) Radial distribution; b) Axial distribution. ($r_s$ = 1.69 mm, 1.38 mm and 1.16 mm; $\Delta\delta_p$ = 0.6 mm, 1.2 mm and 2.4 mm respectively for sample A, B and C).

inverted parabola, apart from sample C which seems to exhibit again a maximum value at $r/r_s \simeq \pm 0.6$. These maximum values were estimated as being 2.8, 2 and 0.9 for samples A, B and C, respectively. The minimum values were located at the surface ($r \simeq r_s$) and it is observed that the higher the applied extension, the weaker the gradient. For sample A, the profile is rather flat around the central part ($0 \leq r/r_s \leq 0.6$) and $S_f$ abruptly drops down at $r/r_s \simeq 0.7$. In the central region of the specimen, voids were mentioned to be initially penny shaped. This is indicated by the shape factor of about 2.8 for sample A: the mode diameter is 3 times greater than the mode height. The mode diameter did not vary so much from sample A to sample B but the mode height increased (Fig. 7a–b). This latter phenomenon is the essential origin of the decrease of the shape factor: from 2.8 to 2. Therefore for sample B, height was increased in such a way that the diameter was twice the height. Concerning sample C, void deformation was observed to be due to both an increase in height and a decrease in diameter. The shape factor was close to unity (height $\leq$ diameter).

To sum up, from sample A to sample B in the central region, the decrease in the shape factor was mostly due to an increase in mode height with the mode diameter remaining constant. Elsewhere, it was due to both decreases in mode diameter and increases in mode height. Note that void volume fraction distribution reported in Cayzac et al. (2013) was always as an inverted parabola which is only similar to the $S_f$ profile for samples A and B.

Fig. 8b depicts the evolution of the shape factor along the $z$-axis for the three samples. The profile is nearly parabolic, except for sample A for which it keeps a constant value of about 2.5. In the central region, the same observations as in the previous paragraph are shown. It is to be noted that whatever the sample, for $z/(\Delta\delta_p) \geq 0.5$, that is near the neck shoulder, the shape factors merge to a constant value estimated at 2.5. In the moving position of the neck shoulder during the stretching, the geometry of void (penny shaped) remained unchanged.

## 4. Discussion: anisotropic volumetric strain

The variations of the mode height and diameter of voids have been quantified in the previous section. The mapping in volume of the specimen was enabled by using the SVOI. An attempt is now made to determine the strain tensor related to the aforementioned variation. As the strain calculation involved a derivative operation, the scattered experimental data, as seen previously, required a fitting procedure based here on the finite element stress field. A direct quantification of the void deformation was performed using local strain tensors. The distributions of the strain tensors through the deformed net section will be discussed.

### *4.1. Finite element modelling: data fitting based on the stress field*

The multiaxial stress state was described by Bridgman (1944) for axisymmetrically notched specimens. These theoretical works yielded the radial distributions of the stress components and the major role determining the void growth was attributed to the stress triaxiality ratio. This work was extended to the $z$-axis by Beremin (1980). The constitutive model used was Von Mises perfectly plastic model applied to metallic materials.

When dealing with damage modelling of Polyamide 11, Boisot et al. (2011) utilized a modified Gurson–Tvergaard–Needleman (GTN) model (Gurson, 1977; Tvergaard, 1982; Tvergaard and Needleman, 1984). Especially, a comparison between analytical Beremin (1980) and porous viscoplastic GTN models was systematically carried out. The result was that, for at least PA11, the Beremin (1980) model successfully captured the plastic dilation up to 3% (at the peak stress).

For the PA6 material under study, Cayzac et al. (2013) implemented a multimechanism model that accounts for damage (void volume fraction) into an in-house FE code Z-set (Besson and Foerch, 1997). Indeed, the net section of samples A, B and C being under multiaxial stress state, FE computations were required. The simulations, although based on isotropic damage, clearly showed the relevance of the constitutive model in terms of both stress-strain curves and distributions of the void volume fractions in the net section. Table 4 recalls the comparison between measured and simulated radii ($r_s$) for each sample. It can be seen that the FE results slightly underestimate $r_s$.

From sample A to B, the void diameter did not change (Section 3.2) whereas the height increased. This mode of deformation was then related to the local stress state obtained by FE computations. If the void diameter did not decrease when a stress was applied in the axial direction, it is supposed that there was a **positive radial stress** within the zone of interest. A first attempt was then made to compare the profiles of radial stresses with the diameter distributions (Fig. 9a) for all samples.

It can be observed that the radial stress distributions were similar to that of the void diameters although the experimental data corresponding to the latter were significantly scattered. The stress values are summarized in Table 4. It can be noted that:

– the stress value that prevented the diameter for decreasing was estimated at 25 MPa (high triaxial stress state);

**Table 4**
Experimental and simulated $\boldsymbol{r_s}$ – Stress levels at $\boldsymbol{r/r_s = 1}$ (notch root) and at $\boldsymbol{r/r_s = 0}$ (centre); $\sigma_r(\mathrm{r}/\mathrm{r_s} = \mathbf{0}) \simeq \mathbf{0}$

| | Exp. $r_s$ | FE $r_s$ | $\sigma_r(r/r_s = 0)$ | $\sigma_z(r/r_s = 0)$ | $\sigma_z(r/r_s = 1)$ |
|---|---|---|---|---|---|
| Sample A | 1.69 mm | 1.54 mm | 25 MPa | 121 MPa | 101 MPa |
| Sample B | 1.38 mm | 1.22 mm | 22.6 MPa | 145 MPa | 168 MPa |
| Sample C | 1.16 mm | 1.08 mm | 4.3 MPa | 153 MPa | 243 MPa |

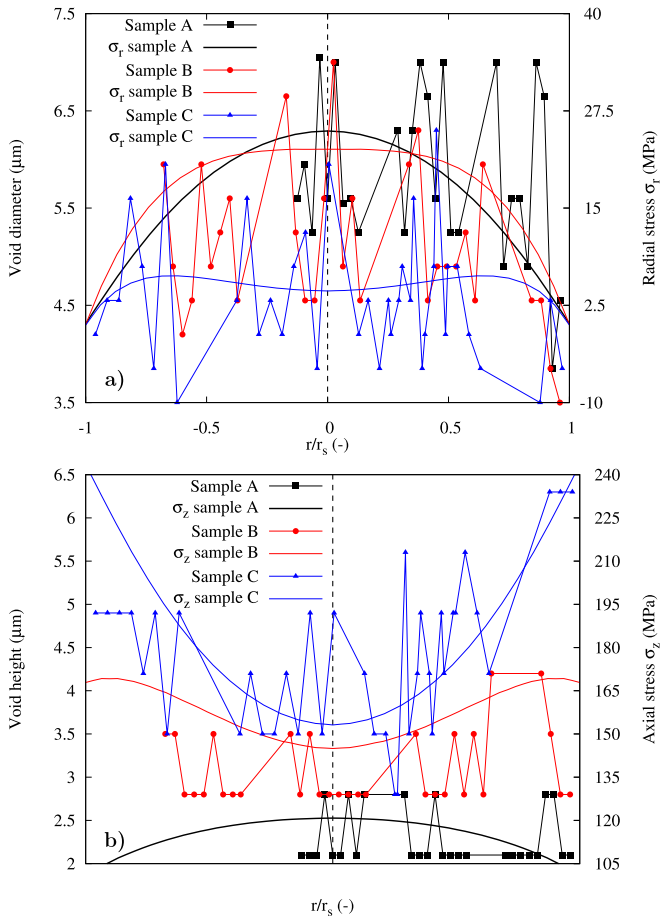


**Fig. 9.** Distributions of void diameter/height and corresponding radial/axial stress for samples A, B and C: a) Void diameter superimposed with radial stress $\sigma_r$; b) Void height superimposed to axial stress $\sigma_z$.

- the radial stress was zero near the notch root whatever the load level (uniaxial stress state);
- $\sigma_r(r/r_s = 0) \simeq 4$ MPa for sample C, meaning that the lateral wall was not stress free with this configuration (moderate triaxial stress state).

Except for sample B where the stress field has been overestimated, the radial stress curves agree well with the profile of the mode diameter.

The same operation was carried out in Fig. 9b for the void height in comparison with the axial stress ($\sigma_z$):

- the axial stress in the centre $\sigma_z(r/r_s = 0)$ continuously increased as a function of the applied displacement (see Table 4 for the stress values);
- the same increase was observed for $\sigma_z(r/r_s = 1)$ but the profile of the $\sigma_z$ distribution varies according to $\Delta\delta_p$: that is an inverted parabola for sample A, two inflexions for sample B and a parabola for sample C.

Both diagrams in Fig. 9 display two *y*-axes consisting of the void mode diameter (*resp.* height) and the radial stress $\sigma_r$ (*resp.* axial stress $\sigma_z$). To smooth the scatter in the measurements of the void characteristic mode lengths, a scaling factor was used between the two *y*-axes. The results are shown in Fig. 7. It can be observed that the trends of void mode diameter and height are in very good agreement with their fitting curves based on $\sigma_r$ and $\sigma_z$ stresses respectively. This enables the void mode diameter and mode height to be obtained as continuous functions of the normalized radial coordinates. By using these stress fits, it is easier to obtain the deformation distributions.

As a consequence of the stress field fitting procedure, the void shape factor $S_f$ related to the stress ratio $\sigma_r/\sigma_z$ was calculated. Fig. 8a shows that the trend of $S_f$ follows closely that of $\sigma_r/\sigma_z$ even if the fitted result underestimates the experimental $S_f$ of sample A. This highlights a relationship between a geometrical parameter and the stress field where the anisotropy is involved.

### 4.2. Local void deformations

The stress fitted profiles allowed the scatter in the experimental data to be smoothed and also, the calculation of the local strain tensor $\underset{\sim}{\boldsymbol{\varepsilon}}$ applied to the voids.

$$\underset{\sim}{\boldsymbol{\varepsilon}} = \begin{pmatrix} \varepsilon_r & 0 & 0 \\ 0 & \varepsilon_\theta & 0 \\ 0 & 0 & \varepsilon_z \end{pmatrix} \tag{1}$$

with $\varepsilon_\theta$ assumed to be equal to $\varepsilon_r$. As sketched in Fig. 10a, two steps were considered in the estimates of strain components: the first (from A to B) takes sample A as the initial configuration whereas the second (from B to C) refers to sample B data.

The total strain tensor components (Eq. (1)) are defined as follows:

$$\varepsilon_r = \frac{\Delta\phi_i}{\phi_{i-1}} \quad \varepsilon_z = \frac{\Delta h_i}{h_{i-1}} \tag{2}$$

where:

- $i$ index is the sample number at the end of the increment: $i$ = B or C;
- $\Delta h_i$ is the increment of void mode height $h$;
- $\Delta\phi_i$ is the increment of the void mode diameter $\phi$.

The volume change defined as the trace of the strain tensor $\underset{\sim}{\boldsymbol{\varepsilon}}$ reduces to:

$$\frac{\Delta V}{V_0} = \varepsilon_z + 2\varepsilon_r \tag{3}$$

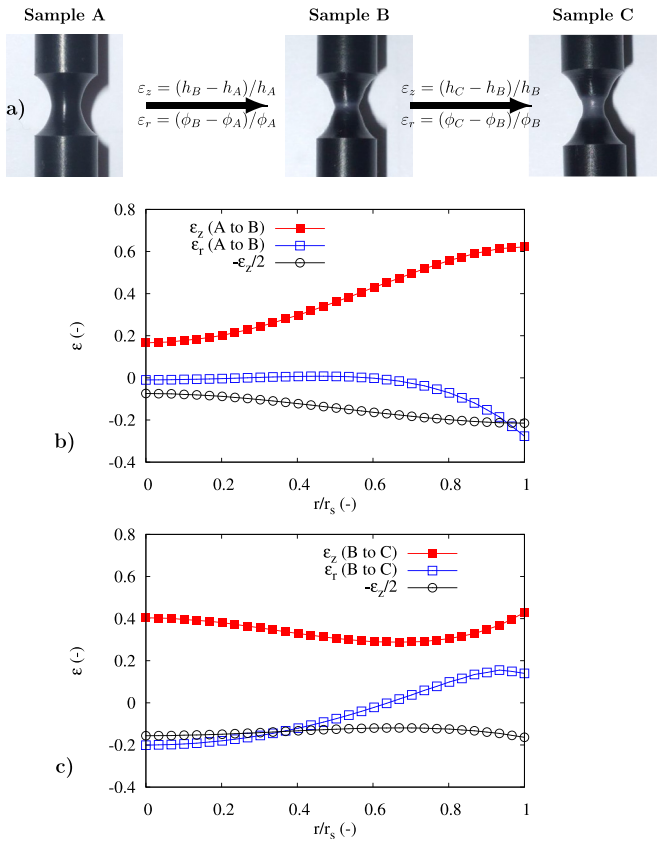


**Fig. 10.** a) Definition of the strains components and the initial configurations: $\boldsymbol{h}_\zeta, \phi_\zeta$ refer respectively to void height and void diameter of sample $\zeta$; b) Void strains distributions from sample A to sample B; c) Void strain distributions from sample B to sample C.

For an isochoric mode of deformation, $\Delta V/V_0 = 0$, yielding:

$$\varepsilon_r \simeq \varepsilon_\theta = -\frac{\varepsilon_z}{2} \tag{4}$$

In the following, the difference between $\varepsilon_r$ and $-\varepsilon_z/2$ (Eq. (4)) is assumed to give a measure of the deviation from an isochoric deformation of the voids.

#### 4.2.1. From sample A to sample B

The distributions of strains during the stress softening stage are shown in Fig. 10b. A gradient of the axial strain $\varepsilon_z$ (full squares) is observed in the radial distribution. The minimum value of about 20% is located in the centre of the net section. The maximum strains, reaching values as high as 60% were observed in the vicinity of the notch root radius. The mean value of $\varepsilon_z$ was then evaluated to be at about 40%.

$\varepsilon_r$ is plotted with open square symbols and the estimation for incompressible material (isochoric deformation) is shown as open circle symbols. The key points of Fig. 10b are summarized as follows:

- for $0 \le r/r_s \le 0.6$: $\varepsilon_z > 0$ and $\varepsilon_r \simeq 0$, there is an axial extension and no radial deformation. A void growth is observed, the volumetric strain increase of which has approximately the same value as $\varepsilon_z$. The maximum volume change is located at $r/r_s \simeq 0.6$ where the difference between $\varepsilon_r$ and $-(\varepsilon_z/2)$ is a maximum;
- for $0.6 \le r/r_s \le 0.9$: $\varepsilon_z > 0$, with $-(\varepsilon_z/2) \le \varepsilon_r \le 0$ meaning that there is a radial contraction of the voids but its magnitude is not high enough to achieve isochoric transformation. There is still void growth but the volumetric strain is less than in the previous region;
- for $r/r_s \ge 0.9$: $\varepsilon_z > 0$ and $\varepsilon_r \le -(\varepsilon_z/2)$. The radial contraction of voids goes further than the isochoric deformation. This would mean voids decreasing in volume. However, it has been mentioned that in this region voids were inclined so that the height is presumably underestimated by the projection operation.

#### 4.2.2. From sample B to sample C

Attention will now be paid to the deformation field during the stress plateau (Fig. 10c).

The radial gradient in $\varepsilon_z$ is less pronounced than in the previous deformation stage. The axial strain is quite homogeneous with values ranging from 0.3 to 0.4. The extension of the necking means that the net section is no longer localized. A small smooth specimen is drawn with a rather uniaxial stress state.

- for $0 \le r/r_s \le 0.4$: $\varepsilon_z > 0$ but $\varepsilon_r \simeq -\varepsilon_z/2$. In this region, voids are subjected to isochoric deformation. Voids have first experienced a volume increase in the previous step;
- for $0.4 \le r/r_s \le 0.6$: $\varepsilon_z > 0$ with $(-\varepsilon_z/2) \le \varepsilon_r \le 0$. As in the previous step, the volume of voids still increases but there is a radial contraction;
- for $r/r_s \ge 0.6$: $\varepsilon_z > 0$ and $\varepsilon_r \ge 0$. Voids are subjected to both radial and axial extension: triaxial void growth is observed. Caution has to be taken in this region due to the inclination of the voids.

To sum up, cylindrical voids in the net section are subjected to a heterogeneous and anisotropic deformation. The deviation from the isochoric transformation has been quantified by comparing the lateral strain $\varepsilon_r$ with $-(\varepsilon_z/2)$.

### 4.3. Plastic dilation

The term *plastic dilation* was defined by Ognedal et al. (2014) in such a way that *plastic* refers to irreversible or permanent strain whereas *dilation* deals with volumetric strain. In this section, an attempt is made to focus on the profile of the heterogeneous void volume change (void growth) within the net section. The evolutions of the space and time of the plastic dilation calculated from the "measured" strains of voids are plotted in Fig. 11.

From sample A to sample B (open squares), that is during the stress softening phase, $\Delta V/V_0 > 0$ meaning that an irreversible volumetric strain exists throughout the net section. Its distribution is not homogeneous. Indeed, it can be seen that in the central part of the net section, the volume increase was about 18% and the maximum value, situated at $r/r_s \simeq 0.7$ is estimated at 42%. The mean value was about 30%, which clearly cannot be neglected (not isochoric).

During the stress plateau, from sample B to sample C (open circles), the plastic dilation distribution increases from the centre of the net section to the surface. The minimum value at the centre being zero meaning that isochoric transformation of the voids operates in this area. The maximum value reaching 70% near the surface has to be considered with caution due to the uncertainties in these regions.

For polymers, several sources of the volume change can be invoked. However, by considering here that this is essentially due the void growth, the volumetric strain can be determined by integrating through the thickness the measurements at the surface. This assumes a homogeneously distributed deformation (Gaucher-Miri et al., 1997; Cangemi et al., 2004; Addiego et al., 2006; Challier et al., 2006). Fig. 11 clearly shows that this is in contrast with the trends of the "measured" plastic

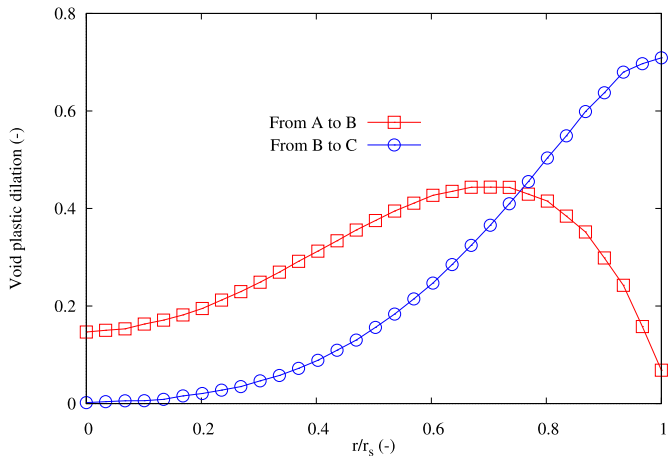


**Fig. 11.** Radial distributions of void plastic dilation: $\Delta \mathbf{V}/\mathbf{V_0} = \varepsilon_\mathbf{z} + \mathbf{2}\varepsilon_\mathbf{r}$.

dilation. The values of the volume change at the surface are close to that obtained at $r/r_s = 1$. Depending on the macroscopic deformation level, the value at the surface is a minimum (from A to B) or a maximum (from B to C). The distributions inside the net section cannot be predicted from these values at the surface. It can be concluded that the tomographic measurements allowed both anisotropy and trough thickness heterogeneity of the plastic dilation to be highlighted.

## 5. Conclusion

This paper deals with the understanding and quantification of the evolution of voids in a deformed semi-crystalline polyamide 6 using 3D image analysis of tomography data. Tensile tests on PA6 axisymmetrically notched round bars were carried out and stopped at three key positions in a stress-strain like curve: at the maximum net stress (sample A), at the end of the stress softening stage (sample B) and at the end of the stress plateau corresponding to the onset of the final failure (sample C).

The volume of interest (VOI) allowing the deformation gradient to be highlighted at the microscopic scale, was evaluated at about 100 spherulites. Statistical data provided within each VOI were used to plot the spacial distribution of the volume fractions of voids and the void mode height/diameter at each deformation stage. This work has confirmed the evolution of the anisotropy index occurring during the deformation. The novelty here consists in the introduction of the void shape factor as a local measure of this anisotropy index. For each deformation stage, the spacial evolution of this shape factor was plotted with the maximum (penny shaped void) at the centre of the net section. The minimum value corresponding to cylindrical void for which the height was larger than the diameter, was obtained near the surface. Here, the most important results were the determination of these maximum/minimum values of the void shape factor instead of an average value of the anisotropy index usually used, through the thickness of the deformed sample.

By fitting the void height and diameter distributions to the stress field simulated by FE modelling, void axial and radial *strains* could be calculated and plotted. The results showed that the axial strain was always positive ranging from 20 to 60%, whereas the radial strain was observed to vary from −30 to 18%. These latter variations indicate that, depending on its location in the net section, a void can increase, decrease or remain constant in volume. The calculation of the irreversible volume change, called plastic dilation exhibited a gradient within the net section. These findings highlight that the volume change measured at the macroscopic scale by full field extensometer using image correlation technique is only limited to surface observations. Moreover, the *homogeneous* correction of the out of plane strain, as commonly used in the literature, is clearly not relevant.

In terms of constitutive modelling, this work has confirmed that it is of prime importance to take into account void growth to correctly predict the state of stress for 3D models. Both microscopic and macroscopic data have to be used to better refine the determination of material parameters. In this way, the micro-mechanisms of deformation have been linked to the macroscopic properties by using a FE inverse optimization method. This will, in turn, improve the prediction of the durability of engineering structures made of polymers, assisted by a FE code.

## References

Addiego, F., Dahoun, A., G'sell, C., Hiver, J., 2006. Characterization of volume strain at large deformation under uniaxial tension in high-density polyethylene. Polymer 47, 4387–4399.

Beremin, F., 1980. Calculs élastoplastiques par la méthode des éléments finis d'éprouvettes axisymétriques entaillées circulairement. J. Méc. Appl. 4, 307–325.

Besson, J., Foerch, R., 1997. Large scale object-oriented finite element code design. Comp. Methods Appl. Mech. Eng. 142, 165–187.

Beucher, S., 1990. Segmentation d'images et morphologie mathématique. Ecole Nationale Supérieure des Mines de Paris (in French). (Ph.D. thesis).
Boisot, G., Laiarinandrasana, L., Besson, J., Fond, C., Hochstetter, G., 2011. Experimental investigations and modeling of volume change induced by void growth in polyamide 11. Int. J. Solids Struct. 48, 2642–2654.
Bridgman, P., 1944. The stress distribution at the neck of a tension specimen. Trans. ASME 32, 553–574.
Brusselle-Dupend, N., Rosenberg, E., Adrien, J., 2011. Characterization of cavitation development while tensile testing pvf2 using 3-d x-ray micro-tomography. J. Mater. Sci. Eng. A 530, 36–50.
Butler, M., Donald, A., AJ, R., 1998. Time resolved simultaneous small- and wide-angle x-ray scattering during polyethylene deformation -ii. cold drawing of linear polyethylene. Polymer 39, 39–52.
Cangemi, L., Elkoun, S., G'Sell, C., Meimon, Y., 2004. Volume strain changes of plasticized poly(vinylidene fluoride) during tensile and creep tests. J. Appl. Polym. Sci. 91, 1784–1791.
Castagnet, S., Girault, S., Gacougnolle, J., Dang, P., 2000. Cavitation in strained pvdf : mechanical and x-rays experimental studies. Polymer 41, 7523–7530.
Cayzac, H., Saï, K., Laiarinandrasana, L., 2013. Damage based constitutive relationships in semi-crystalline polymer by using multi-mechanisms model. Int. J. Plast. 51, 47–64.
Challier, M., Besson, J., Laiarinandrasana, L., Piques, R., 2006. Damage and fracture of polyvinylidene fluoride (PVDF) at 20 °C: Experiments and modelling. Eng. Fract. Mech. 73, 79–90.
Chaudemanche, S., Ponçot, M., André, S., Dahoun, A., Bourson, P., 2014. Evolution of the raman backscattered intensity used to analyze the mechanisms of deformation of various polypropylene blends in situ during a uniaxial tensile test. J. Raman Spectrosc. 45, 369–376.
Farge, L., André, S., Pawlak, P., Baravian, C., Irvine, S., Philippe, A., 2013. A study of the deformation-induced whitening phenomenon for cavitating and non-cavitating semicrystalline polymers. J. Polym. Sci. Part B Polym. Phys. 51, 826–841.
Feret, L., 1930. La grosseur des grains des matières pulvérulentes. Premières Commun. la Nouv. Assoc. Int. l'essai matér., groupe D 428–436.
Gaucher-Miri, V., Depecker, C., Séguéla, R., 1997. Reversible strain-induced order in the amorphous phase of a low-density ehylene/butene copolymer. J. Polym. Sci. Part B. 35, 2151–2159.
Gurson, A., 1977. Continuum theory of ductile rupture by void nucleation and growth: part1: yield criteria and flow rules for porous ductile media. J. Eng. Mater. Technol. 99, 2–15.
Hughes, D., Mahendrasingam, A., Oatway, W., Heeley, E., Martin, C., Fuller, W., 1997. A simultaneous saxs/waxs and stress-strain study of polyethylene deformation at high strain rates. Polymer 38, 6261–6432.
Laiarinandrasana, L., Morgeneyer, T., Proudhon, H., N'Yguyen, F., Maire, E., 2012. Effect of multiaxial stress state on morphology and spatial distribution of voids in deformed semicrystalline polymer assessed by x-ray tomography. Macromolecules 45, 4658–4668.
Laiarinandrasana, L., Morgeneyer, T., Proudhon, H., Regrain, C., 2010. Damage of semicrystalline polyamide 6 assessed by 3D X-ray tomography: from microstructural evolution to constitutive modeling. J. Polym. Sci. Pol. Phys. 48, 1516–1525.
Landron, C., Maire, E., Bouaziz, O., Adrien, J., Lecarme, L., Baggeri, A., 2011. Validation of void growth models using x-ray microtomography characterization of damage in dual phase steels. Acta Mater. 59, 7564–7573.
Morgeneyer, T., Proudhon, H., Cloetens, P., Ludwig, W., Roirand, Q., Laiarinandrasana, L., Maire, E., 2014. Nanovoid morphology and distribution in deformed hdpe studied by magnified synchrotron radiation holotomography. Polymer 55, 5439–5443.
Ognedal, S., Clausen, A., Dahlen, A., Hopperstad, O., 2014. Behavior of pvc and hdpe under highly triaxial stress states: an experimental and numerical study. Mech. Mater. 72, 94–108.
Pawlak, A., Galeski, A., 2008. Cavitation during tensile deformation of polypropylene. Macromolecules 41, 2839–2851.
Pawlak, A., Galeski, A., 2010. Cavitation and morphological changes in polypropylene deformed at elevated temperatures. J. Polym. Sci. Part B Polym. Phys. 48, 1271–1280.
Peterlin, A., 1971. Molecular model of drawing polyethylene and polypropylene. J. Mater. Sci. 6, 490–508.
Regrain, C., Laiarinandrasana, L., Toillon, S., Saï, K., 2009. Multi-mechanism models for semi-crystalline polymer: constitutive relations and finite element implementation. Int. J. Plast. 25, 1253–1279.
Rozanski, A., Galeski, A., 2013. Plastic yielding of semicrystalline polymers affected by amorphous phase. Int. J. Plast. 41, 14–29.
Schultz, J., 1974. Review: deformation mechanisms in crystalline polymers. Polym. Mater. Sci. 2034–2051.
Serra, J., 1988. Image Analysis and Mathematical Morphology, vol. 2. Academic Press, London.
Tvergaard, V., 1982. On localization in ductile materials containing spherical voids. Int. J. Fract. 18, 237–252.
Tvergaard, V., Needleman, A., 1984. Analysis of the cupcone fracture in a round tensile bar. Acta Metall. Mater. 32, 157–169.
Xiong, B., Lame, O., Chenal, J., Rochas, C., Séguéla, R., Vigier, G., 2013. In-situ saxs study and modeling of cavitation/crystal-shear competition in semi-crystalline polymers: influence of temperature and microstructure in polyethylene. Polymer 54, 5408–5418.

## Nomenclature

*DIC:* Digital image correlation
$\Delta\delta_p$*:* Permanent set of the specimen after unloading
$\delta_0$*:* Initial opening displacement (gauge length)
$\boldsymbol{\varepsilon}$*:* strain tensor
*ÈSRF:* European synchrotron radiation facility
*F:* Load
*FE:* Finite element
$\phi$*:* Void mode diameter
*GTN:* Gurson–Tvergaard–Needleman model
*h:* Void mode height
$h_w$*:* Height of the whitened zone in the necking region
*IPSLT:* Incoherent polarized steady light transport
*MDSC:* Modulated differential scanning calorimetry
*PA6:* Polyamide 6 polymeric material
*PA11:* Polyamide 11 polymeric material
*r:* Current distance from the centre of the net section (0 < r < rs)
$r_s$, $r_0$*:* Radius of the deformed net section, initial radius of the net section
$S_0$*:* Initial net section area
*SAXS:* Short angle X-ray scattering
*SEM:* Scanning electron microscope
$S_f$*:* Void shape factor
*SRT:* Synchrotron radiation tomography
*SV OI:* Statistical volume of interest
$\underline{\underline{\sigma}}$*:* Cauchy stress tensor
*TEM:* Transmission electron microscope
$T_g$*:* Glass transition temperature

$T_m$: Melting point temperature
$\tau_s$: Stress triaxiality ratio
*TV OI:* Tomographic volume of interest
$V$, $V_0$: Current volume, initial volume at the macroscopic scale
$\chi$: Index of crystallinity